Heisenberg Model Analysis on Inelastic Powder Neutron Scattering Data Using Parent and K Doped $BaMn_2As_2$ samples

M. Ramazanoglu,[1,2] A. Sapkota,[3,4] A. Pandey,[3,4,*] J. Lamsal,[3,4] D. L. Abernathy,[5]

J. L. Niedziela,[5] M. B. Stone,[5] R. Salci,[1] D. A. Acar,[1] F. O. Oztirpan,[1] S. Ozonder,[1]

A. Kreyssig,[3,4] A. I. Goldman,[3,4] D. C. Johnston,[3,4] and R. J. McQueeney[3,4]

[1] *Physics Engineering Department, Istanbul Technical University, 34469, Maslak, Istanbul, Turkey*
[2] *Tübitak BİDEP 2232 Fellow, Ankara, 06100, Turkey*
[3] *Ames Laboratory, Ames, IA, 50011, USA*
[4] *Department of Physics and Astronomy, Iowa State University, Ames, IA, 50011, USA*
[5] *Quantum Condensed Matter Division, Oak Ridge National Laboratory, Oak Ridge, TN, 37831, USA*
(Dated: August 19th,2017)

Low temperature powder inelastic neutron scattering measurements were performed on three different powder samples; parent $BaMn_2As_2$,12.5 % K-doped $Ba_{.875}K_{0.125}Mn_2As_2$ and 25 % K-doped $Ba_{(.75)}K_{0.25}Mn_2As_2$. The Heisenberg Model involving J_1-J_2-J_z coupling constants were compared to the data by a powder integration routine using Monte Carlo integration methods. The best magnetic parameters were selected using a chi-square test where model intensities were compared to the full (q,E) dependence of magnetic scattering. A key step to this analysis is the characterization of the background which is formed mostly by phonon scattering intensities along with other sources including the magnetic impurity scattering events. The calculated powder magnetic intensities added to the estimated background obtained from the non-magnetic high momentum transfer region. The agreement between the simulated and the raw data enabled us to perform quantitative analysis of the unreacted MnO impurities. Overall, this is another confirmation along with earlier studies using this technique, that magnetic exchange constants can be calculated within an acceptable range with a very quick inelastic neutron powder experiment without need for a single crystal sample.

INTRODUCTION

Ever since the discovery of pnictide -Fe based-high temperature superconductors , the parent compounds which are usually anti-ferromagnetic (AFM) and non-superconducting materials became a topical subject to study the mechanism which develops superconductivity[1]. $BaMn_2As_2$ is one of these parents - even though there is not any superconducting offspring-, studied in this article. $BaMn_2As_2$, as the parent compound, is a G-type AFM insulator with a Néel transition temperature at T_N=625 K [2–5]. It is chemically an isostructural compound to $BaFe_2As_2$ which is the parent of the well-known family of iron pnictide superconductors. The charge carrier concentration variation in the AFM parents, which are usually semiconductors or insulators, yields a stabilization of metallic behaviour as a result [2–5]. This metalization and its effect on magnetic excitations are the current subjects in this article studied on K-doped $Ba_{1-x}K_xMn_2As_2$.

The doped isostructural $BaFe_2As_2$ was studied extensively with various techniques [4]. The increasing concentrations of either electron or hole carriers suppresses the AFM stripe order yielding a superconducting state with a dome in their phase diagram. In $BaFe_{2-x}Co_xAs_2$ and $BaFe_{2-x}Ni_xAs_2$ Fe ion sites are replaced by transition metal ions of Co and Ni, respectively [6–8]. This doping induces electron carrier density to the parent compound of $BaFe_2As_2$. On the other hand, hole doping can be created by diluting the Ba sites with K in $Ba_{1-x}K_xFe_2As_2$

[9, 10]. With this property they resemble the copper oxide superconductors very much. These compounds show that the electronic properties of the $3d$ shell determine itinerant magnetic behavior and overall physical state of the material [6–8].

Magnetic susceptibility, resistivity, ARPES and heat capacity measurements show that parent $BaMn_2As_2$ is an AFM insulator [2, 3]. The AFM state has a local moment behavior in comparison to the more itinerant behavior seen in Fe 122 compounds. A well defined charge gap is measured for this compound using optical spectroscopy which attests the well developed insulating state [11]. The results of these measurements are analyzed by dynamical mean field theory calculations showing that the $BaMn_2As_2$ compound is a member of Mott-Hund insulators, resembling to copper based superconductors.

This property puts $BaMn_2As_2$ in a special place like a bridge between itinerant, iron based superconductors and local moment copper based superconductors. Therefore studying the magnetism of $BaMn_2As_2$ becomes more critical on the path to understanding the unconventional superconductivity. However this prosaic subject becomes more interesting with hole doping. While weakly K doped samples show metallic behaviour even without disturbing the parent AFM state highly K doped ones show weak FM metallic properties[3, 5].

In this article we aim to study the change in the magnetic excitations of polycrystalline K doped $Ba_{1-x}K_xMn_2As_2$ samples with x=.125 and .25 with respect to the parent compound ; $BaMn_2As_2$. Usually

these kind of magnetic studies are done using single crystal inelastic neutron scattering (INS) technique, but here we want to show that such a study can also be possible using powder. In the previous publication[12], the magnetic excitations were analyzed with similar but yet a different method. In that manuscript, the magnetic INS was calculated by the Heisenberg Spin Model with Monte-Carlo integrations as presented below. However, the fits to the data were performed on the momentum-averaged energy spectra without considering the q dependent variations of the scattering. Here, we retain and fit the full q and E dependence and perform global fits to the entire magnetic scattering data range. Like the previous method, this method depends critically on estimating the background spectrum due mainly to the phonon and magnetic impurity scattering. This estimated background, unlike the previous method, will be added to the calculated spectrum and fit to the INS data. We compare the estimation of Heisenberg exchange parameters of both methods at the conclusion of the paper.

EXPERIMENT DETAILS

INS measurements were performed on the powders of $BaMn_2As_2$ and K doped $Ba_{1-x}K_xMn_2As_2$. $BaMn_2As_2$ has a body centered tetragonal (bct) I4/mmm unit cell structure with the lattice constants; a≃4.154 Å and c≃13.415 Å[15]. Two different doped samples were prepared for this measurement which contains 12.5 % K ; $Ba_{0.875}K_{0.125}Mn_2As_2$ and 25 % K ; $Ba_{0.75}K_{0.25}Mn_2As_2$. The ARCS powder neutron spectrometer at Oak Ridge National Laboratory was used to collect INS profiles of these powders at a temperature of 5 K. The powders were prepared by conventional solid-state reaction method and each sample was weighted at roughly 7 grams in mass and packed into cylindrical aluminum cans. INS spectra were measured with different incident energies (Ei) of 30, 74 and 144.7 to 315 meV. The time of flight data was reduced into energy transfer (E) and momentum transfer (q) profiles and data correction for detector efficiency and the empty aluminum can subtraction was performed. The S(q,E) scattering profiles and constant energy/momentum cuts, averaged and binned data were obtained using MSLICE under DAVE software [20].

INELASTIC POWDER MEASUREMENTS AND ANALYSIS

The AFM structure showing G-type ordering was analyzed using J_1-J_2-J_z Heisenberg Spin Hamiltonian model[2, 13]. Here, J_1 and J_2 are the in-plane nearest and next nearest neighbour AFM exchange interaction constants and J_z is the out of plane nearest neighbour interaction. This Hamiltonian is written as;

$$H = J_1 \sum_{NN} \mathbf{S}_i \cdot \mathbf{S}_j + J_2 \sum_{NNN} \mathbf{S}_i \cdot \mathbf{S}_j \\ + J_z \sum_{NN} \mathbf{S}_i \cdot \mathbf{S}_j - D \sum_i (S_i^z)^2 \tag{1}$$

The last term in Eq. (1) is given to denote the single-ion anisotropy where D is the uniaxial anisotropy parameter for Mn^{+2} ion.

In this article, like in reference [2, 12], the AFM interactions are represented by positive $J_i > 0$ and calculations were conducted for the product of SJ . Out of 5 competing magnetic states, for zero applied field, G-type AFM ground state energy is given by Eq. (2)

$$E_{Gtype} = NS^2(-2J_1 - J_z + 2J_2) \tag{2}$$

where N is the total number of spins. According to the calculations between the possible ground states, the expression given in Eq. (2) is found to be the lowest energy state with the following restriction for a G-type AFM ground state; $J_1 > 0$, $J_1 > 2|J_2|$ and $J_z > 0$. Notice the restrictions on the magnetic exchange constants where J_1 and J_z are only anti-ferromagnetic (meaning positive) while J_2 can be either ferromagnetic or anti-ferromagnetic [2]. Antiferromagnetic J_2 frustrates the magnetic ordering in the (ab) plane.

In order to simulate the INS spectrum of S(q,E) we use the Heisenberg Hamiltonian model, given in Eq. (1). This equation is solved, in linear spin-wave approximation, by rewriting all terms in terms of the Holstein-Primakoff representation involving the boson spin operators. The Fourier transform of the boson operators, we yields the following spin-wave dispersion relations for G-type AFM structure;

$$\hbar\omega(\mathbf{q}) = 2SJ_1 \left(\{2 + \frac{J_z}{J_1} - \frac{J_2}{J_1}[2 - \cos(q_x a) - \cos(q_y a)]\}^2 \right.$$

$$\left. - \{\cos\left((q_x + q_y)\frac{a}{2}\right) + \cos\left((q_x - q_y)\frac{a}{2}\right) + \frac{J_z}{J_1}\cos(\frac{q_z c}{2})\}^2 \right)^{\frac{1}{2}} \tag{3}$$

and for qa ≪ 1

$$\hbar\omega(\mathbf{q}) = \hbar\left(V_{ab}^2(q_x^2 + q_y^2) + V_c^2 q_z^2\right)^{\frac{1}{2}} \tag{4}$$

where $\hbar$ is the Planck constant, V_{ab} and V_c are the spin-wave velocities in the (ab) plane and along the c crystalline direction, respectively. These velocities can also be derived in term of magnetic exchange constants as

$$\hbar V_{ab} = 2J_1 Sa \left((1 - \frac{2J_2}{J_1})(1 + \frac{J_z}{2J_1}) \right)^{\frac{1}{2}}$$

(5)

$$\hbar V_c = \sqrt{2} J_1 Sc \left((\frac{J_z}{J_1})(1 + \frac{J_z}{2J_1}) \right)^{\frac{1}{2}}$$

A detailed derivation for these equalities can be found elsewhere [2, 12, 13].

The results of powder inelastic neutron scattering (INS) measurements ,conducted at T=5 K, are shown in Fig.1. As also explained in the caption of this figure, the panels show the parent and the two different concentrations of K doped $BaMn_2As_2$ sample powders. The incident neutron beam energy is E_i =74 meV for the panels on the left of the figure (a,b and c) while it is 144.7 meV for the right side panels (d,e and f). These figures show INS profiles for whole possible energy and momentum ranges for each experimental configuration. The dominant or the most eye catching property in these panels is the higher intensity values as the q momentum transfer increases especially for E≤40 meV region. Even though these unpolarized INS intensities are created by powder averaged inelastic scattering events from lattice and magnetic excitations, one can distinguish, the dispersive spectra between magnons and phonons by their different q (momentum transfer) dependences. Therefore, isolating magnetic intensities from phonon contamination becomes the essential basis for this study. To achieve this step, the different characteristic q dependences for magnetic and phonon scattering were used. The magnetic intensity falls off with q, obeying the magnetic form factor's exponential dependence on q, while phonon intensities increase as, q^2. The high intensities observed on the high q side and low E transfer E<40 meV are mostly due to phonon related scattering events. These features will be discussed in detail in the following figures. Another feature in the raw data is the steep intensity bars at around q≃1 $Å^{-1}$ and 2 $Å^{-1}$ which have magnetic scattering origins. The two intensities are spin-waves originating in the vicinity of magnetic reflections of (101) and (103) [15]. This is confirmed by calculating the corresponding q values of these 2 reflections which coincide with the values shown in Fig.2.

Since our interest is to study the magnetic INS profile, we only focused on the low q side of the data since this region where the magnetic scattering is present. Thus the low-q INS profiles, shown in Fig.2, are obtained for E_i =144.7 meV data. In this figure, panel (a) shows the parent $BaMn_2As_2$ INS data while panel (b) and (c) show 12.5 % and 25 % K doped $Ba_{(1-x)}K_xMn_2As_2$ INS data, respectively.

In panels (a,b and c) of Fig.2, the main feature is the two steep excitations which are seen up to E≃50 meV. These two reflections occur at the momentum transfer values of q≃1.58 Å and q≃2.06 Å which are the q values for (101) and (103) magnetic reflections of $BaMn_2As_2$[15]. The steep magnetic excitations are the acoustic spin-waves centered at these AFM reflections. A very rough estimate for AFM spin-wave velocity near the (101) peak position yields ⟨V⟩ ≃220 meV/Å. As can be seen, the main features and dispersions are similar for K doped samples, however extra scattering intensities forming weak dispersions are observed in the doped samples due to MnO impurities.

Using Eq.3, we conducted a powder integration Monte-Carlo routine and able to fit the INS spectrum, shown in panels of (aa) to (cc) in Fig. 2. The details of the fit analysis including the background definitions and impurities will be discussed below. As seen from this figure, the magnetic dispersions are dominant for the q≤∼4 $Å^{-1}$ and for ∼50meV≤E≤∼80meV energy transfer regions while the E≤40meV regime is a mixture of magnetic and phonon dispersion intensities. Therefore, for our interest during the analysis is concentrated mostly on q=0.5 $Å^{-1}$to 4.0$Å^{-1}$ region with 10meV≤E≤104meV energy transfer values.

To estimate the phonon background, a line-shape involving ∼ 6 Gaussian is fitted for each sample in the limits of 6≤q≤8$Å^{-1}$ for 0≤E≤150meV, shown in Fig. 3 panel (b). The results of these fits are scaled accordingly with q^2 and is used to create S(q,E) data. An incoherent approximation is used to define an overall phonon background for the region of interest; q=0.5 $Å^{-1}$ to 4.0 $Å^{-1}$. This creates a slowly varying constant background. The estimation of phonon background is also supported by separately fitted constant energy scans of several energy values between 10 meV and 40 meV with a quadratic line shape of q. This is shown in Fig.4, as the energy transfer increases, the slope of the obtained behaviour decreases. For the energy transfer values E≥50meV , a constant background value is used.

With the well-known ∼q^2 behaviour, typical for a single phonon scattering event, and the constant background for the E≥50meV region, we estimate a total background definition, shown in Fig.5. This is used for the analysis of parent compound.

It has been observed that increasing the K doping amount in the samples, increases the possibility of having MnO impurities. Therefore, the calculations of the expected spin-wave scattering for parent MnO powder were performed on the basis of published Heisenberg exchange constants [21]. This is shown in Fig. 3 panel (a). As seen, the only existent magnetic intensities are found in the E≤25 meV region. Thus these calculated magnetic intensities of MnO powder are scaled with ∼ 0.3 % and ∼ 0.7 % for 12.5 % and 25 % K doped samples, respectively, and is used to added on the phonon background values. The calculated intensities in the vicinity of q∼1 A^{-1} is used to match the corresponding q intensities of the raw data.

To sum up, adding the background intensities obtained from MnO calculations and quadratic q dependent fittings for the E≤40 meV range plus the constant background for E≥50meV region, defines an overall estimated complete background for our data analysis which involves magnetic impurities, single and multi-phonon scattering events and the intensities of other complicated scattering events. It should be noted that despite these efforts to define background intensities simply to subtract from the raw data or to add on the calculated magnetic intensities, the absolute background definition can still be improved. These simple estimations and assumptions are only the first step for a complete definition of a real background. Because of the coherent nature of the phonon scattering, including other possible magnetic and lattice based impurities and the Debye Waller factor, may lead to some uncertainties in the low q phonon scattering correction used in this study.

We are now in a position to fit the magnetic data. The Heisenberg Model spin-wave calculations were performed for different sets of SJ_1, SJ_2 and SJ_z values and integrated by Monte Carlo routines. These calculations were done for all the possible AFM SJ parameters, namely $SJ_z > 0$ and $SJ_1 > 2SJ_2$, as discussed before. The intensities in the whole (q,E) space were then compared with magnetic contribution to the INS data using a simple chi-squared, χ^2 test. This is in fact a classical χ^2 grid-search technique. Our parameter search space is based on SJ_1, SJ_2 and SJ_z magnetic coupling constant parameters. The grid-search technique, being one of the oldest methods of fitting compared to the modern non-linear least squares methods, it has the opportunity of catching the local χ^2 minima and being more flexible around them. In other words, while Newton and/or Levenberg-Marquardt techniques may end up being trapped to a local minimum, the grid-search technique tries fitting parameters over a big space of and gives the operator a chance to compare and find the real χ^2 minimum, if there is one. As a matter of fact, this analysis will result in a valley of χ^2 minima in this work. This will be discussed in the last section of this article.

In the first step, the powder averaged magnetic intensities were created with 5000 Monte Carlo sampling points. The integration on each q sphere is calculated for momentum values between q=0.5 Å^{-1} to q=4.0 Å^{-1} with a fine step of q$_{step}$ =0.025 Å^{-1}. For every set of SJs, we calculate a χ^2 value. This way we obtained the best fit parameters of each SJs set. Depending on the best ∼20 results, a higher quality powder-average analysis involving 25000 Monte Carlo integrations for each q sphere were conducted. It was observed that there is a strong dependence of the χ^2 values on SJ_z. Therefore, the best values for SJ_z were considerably faster and easier to determine than the other parameters. Since this is a grid-search fit technique, the process of trying all of the

Table I: Energy scales and magnetic parameters of $Ba_{1-x}K_xMn_2As_2$ as a function of composition. k_BT_N is the actual Néel temperature measured by neutron diffraction. $\langle E \rangle$ was determined numerically from Fig. 9. The magnetic exchange constant values; SJ's were determined by the results of Heisenberg spin-wave fit analysis, as explained in the text.

Composition	$x = 0$	$x = 0.125$	$x = 0.25$
k_BT_N (meV) [15]	53.9±.1	52.7±.3	49.6±.3
$\langle E \rangle$ (meV)	61 ±2	60±2	54±2
SJ_1 (meV)	38±2	41±2	39±2
SJ_2 (meV)	12±1	14±2	13±1
SJ_c (meV)	2±1	3±1	2±1

parameters took an extended time period. However the positive side of this long process is to try and see all of the parameters and to be able to map the χ^2 space with respect to all fitting parameters. This undoubtedly gives us a chance of catching the best parameters no matter how the local minima are placed in the parameter space where a regular non-linear least squares fit technique may create problems. As a result, the best magnetic coupling constants were calculated and given in Table I. The fit results were also shown within detail q cuts profiles in the panels of Fig.6,7,8. These figures were created for the parent (Fig.6) and K doped samples (Fig.7,8). It should be emphasized that intensities over the 50 meV region should mostly be of magnetic origin so that our calculations which are shown in Fig. 2 panel (aa) to (cc) and Fig. 6, 7 and 8 collect almost all of the dispersions in the data with reasonable agreement. The agreement of the simulated intensities to the raw data especially for low (q,E) region for the 25 % K doped sample led the calculation of MnO impurity volume amount in the samples. This point is needed to be underlined because it shows the quality of the analysis technique used in this work.

Our fit results can be compared in the q averaged energy profiles as shown in Fig.9 over the energy transfer axis from E=10 meV to ∼110 meV. The K doping reveals small changes in the intensity profile which can be seen clearly from the q-binned spectrum. In this figure, the INS raw data is shown by red points while the results of the Heisenberg spin-wave calculations are given by blue color line. The green color line shows the the overall fit results where the background with calculated MnO intensities are added to the magnetic calculations. As can be seen, monotonically increasing signal after ∼20 meV has a peak at around 80-90 meV range with a magnetic signal extends up to E∼110 meV. A simple, not shown, Gaussian fit for these signals shows that as K increases, the peak line-shape shifts to the lower energies and gets broader. This can be seen by eye especially when the 25 % K doped sample profile (panel (c)) is compared with the parent the one (panel (a)). This conclusion is sup-

ported by the net decrease in the calculated averaged energy values; $<E>$, shown in Table I. In this table, corresponding Néel Order temperatures, T_N are also given which supports this conclusion as well.

In order to depict the calculated χ^2 behaviour Fig.10 was drawn with SJ_1 vs SJ_2 where SJ_z=2 meV; the best fit values for the parent compound. Here, χ^2 values were represented by a color scale from blue being the minimum, to red being the maximum. As can be seen, calculated χ^2 values produce a minimal valley where both sides of the minimal area are surrounded by a steep hill specifically for the low SJ_1 regime. Similar behaviour was also observed for other samples as well. The black line drawn in this valley can be given by $J_1=\frac{3SJ_2}{2}$-15+0.8J_z representing the minimal region. In one of the previous studies the same analysis was conducted on parent $BaMn_2As_2$ powders, SJ_1,SJ_2 and SJ_z were estimated as 33±3 meV, 9.5±1.3 meV and 3±0.6 meV , respectively [2]. When we compare our results with the previous ones we can easily confirm that the previous results are one of our good-valley values shown in Fig.10. Therefore, we conclude that our current results are in good agreement with those previously published[2, 12].

In order to determine the spin energy gap, $\triangle$ parameter, q momentum cut profiles at q=1.575Å^{-1} and q=2.04Å^{-1} were obtained from E_i =144.7 meV data. For this analysis, the phonon background and the Gaussian fit for the elastic scattering intensities were subtracted [12]. As seen from panels of Fig.11, the intensity profile now has a sharp onset starting with the energy transfer value at ∼5 meV. The big errorbars below this energy value are created due to the uncertainties in the subtraction of the elastic Gaussian fit and the estimated background. A damped harmonic oscillator (DHO) lineshape given in Eq. (6) was used to fit the data[12, 14].

$$S(q, E) = \frac{AE'\Gamma}{(\Gamma^2 + E^2)(1 - e^{(\frac{E}{k_B T})})} \quad (6)$$

where E$'$ is given by;

$$E' = (E^2 - \triangle^2)^{\frac{1}{2}}. \quad (7)$$

Here, A is the amplitude and E is the energy transfer values. Since this lineshape is modeled after (DHO), Γ is the damping constant [14]. $\triangle$ is the spin energy gap while $(1 - e^{(\frac{E}{k_B T})})$ accounts for the Debye temperature effect on the observed intensities. In order to increase the certainty, global fits were performed to the data obtained from those two q cuts where Γ and $\triangle$ were fit to the same values with the same errorbars. The results of this analysis are shown in Table II.

As the final step to confirm the existence of the MnO unreacted impurity phase, especially in our K doped samples, we performed a final X-ray diffraction (XRD) mea-

Table II: The results of line-shape analysis given in Eq. (6). For this analysis, INS profile shown in Fig.11, obtained from E_i =144.7 meV data were used. Parameters of Δ; spin-gap and Γ; DHO damping constant were given in meV units.

Composition	$x = 0$	$x = 0.125$	$x = 0.25$
Δ (meV)	5.41±.23	6.53±.15	6.24±.05
Γ (meV)	17.6±1.2	13.1±.9	14±1

surement on all samples[12]. A Rigaku Geigerlfex powder diffractometer with Cu_{K_α} radiation was used. FULL-PROF Rietveld refinements yielded the existence of MnO powders with 0.12 % and 0.6 % weight percentages for 12.5 % and 25 % K doped samples, respectively[27]. These values are very close to the ones that we used in the analysis.

CONCLUSION AND DISCUSSION

During the Heisenberg spin-wave analysis, it was observed that not only calculating the magnetic intensity, S(q,E) is important, but also defining a complete set of phonon background is essential. The agreement between the fit and the powder data is shown in the constant q cuts of the panels of Figs. 6,7, and 8. Especially, during the χ^2 grid-search, being able to define MnO unreacted powder impurities in our samples indicates the quality and sensitivity of our lineshape analysis. The same conclusion can also be drawn from the data shown in Fig.9 where the q averaged I vs E profiles were given for the magnetic fit with and without background. These are in green and blue circles, respectively. Here the background is composed of the estimated phonon and the calculated magnetic scattering intensities for MnO impurities. The overlap seen for the green and red circles especially for the low energy transfer region confirms the quality of the background estimations in our analysis.

However, when we compare the results of the previous method [12] , the current fits fail to define the raw data especially for the energy region of E∼70 to 90 meV especially for the K doped samples in Fig.7 and Fig.8. Since the analysis we performed in this work is based on the grid-search technique, the step-size of the grid is the main source for determining the best fit parameters. Thus, more fit trials with finer SJ grid step-size are needed to improve the quality of the fits. Here we can count another reason which is the number of q spheres as they decrease in the calculations with increasing energy due to the kinematic limits. This can be seen in Fig.2. As the energy increases, the number of calculations which could be compared to the data used in the χ^2 tests decreases so that our fits become overall less sensitive to the high energy transfer values. Therefore our fits, shown in Fig.9 are better looking for E<80 meV region. The fits of

the previous work[12] were performed in the q-averaged spectrum where this was not the issue and the quality was better than our current results.

The Monte-Carlo integration of the spin-wave Heisenberg model given in Eq. (3) was performed against a set of SJ_1,SJ_2 and SJ_z as explained in the analysis section. The best SJ values obtained from these calculations are given in Table I. Using the equations given in Eq. (4) for spin-wave velocities, we calculated the corresponding velocities in the (ab) plane and along the c direction. The calculated velocities using the best set of SJs for parent powder are $V_{ab} \simeq 194$ meV/Å and $V_c \simeq 167$ meV/Å. From these values, we can reach the powder average spin velocity value of $< V >= \sqrt{V_{ab}^2 + V_c^2} \simeq 256$ meV/Å. This value is very close to the visually estimated value of ~ 220 meV/Å as discussed earlier in the text.

The spin-gap values given in Table II for K doped samples do not show a decrease as the K doping amount increases. This would not have been expected metallic behavior from the doped samples with respect to the parent one. The decrease in the measured T_N values are given in TableII [15]. From the parent to 25 % K doped sample, T_N values drop by only ~ 7 %, which is not a significant change. In other words, we can conclude that such a small change would be hard to observe from a powder INS experiment. When we compare the results of DHO analysis with the results of previous work [12] where E_i =74 meV INS were used, the calculated spin-gap, Δ and the damping constant, Γ values are very similar within the errorbars. This shows the consistency of the DHO analysis.

The analysis of fitting whole (q,E) space compared with q averaged technique used in the previous work[12] yielded very similar results. This is shown as the comparison in Fig. 12 for all of the fitting parameters with respect to K doping percentages. However, there is still a slight increase in the disagreement seen in SJ values especially with K doped samples. Overall agreement shown in this figure ensures the consistency and quality of the two analyses with the quantitative and the qualitative analysis of the amount of MnO impurities. In the previous work[12], the fits were conducted in the q averaged space, where a detailed error-bar calculation was possible for the SJ values. On the other hand, for both works, the previous and the current, a χ^2 grid-analysis conducted over a large sets of SJ values which searches for the best SJs value covers a big SJ parameter space. Thus, we were able to detect the existence of the uniqueness issue in our Heisenberg Spin Model analysis. In other words, calculated SJ parameters in the vicinity of the minimum χ^2 valley, shown in Fig.10, are good with one being considered the same as another. Therefore, the current and the previous techniques are complementary to each other in general. Our current results also confirm the previous analysis results [2].

To summarize, AFM Heisenberg spin-wave analysis was conducted on INS data obtained from $BaMn_2As_2$ and K doped $Ba_{1-x}K_xMn_2As_2$ powders with x=12.5% and x=25%. Depending on the results of the Monte-Carlo study, we could define the magnetic exchange constants, within some uncertainties, and the amount of the magnetic impurity of MnO powders. The magnetic peak profiles were obtained in the view of a quadratic phonon background estimation. Damped harmonic line-shape analysis yields the energy gap values.

ACKNOWLEDGEMENTS

———————

* Present address: Department of Physics and Astronomy, Texas A&M University, College Station, TX 77843, USA

[1] K. Kamihara, T. Watanabe, M. Hirano, and H. Hosono, J. Am. Chem. Soc. **130**, 3296, 2008

[2] D.C. Johnston, R.J. McQueeney, B. Lake, A. Honecker, M.E. Zhitomirsky, R. Nath, Y. Furukawa, V.P. Antopov, Yogesh Singh, Phys. Rev. B **84**, 094445 (2011)

[3] A. Pandey, R.S. Dhaka, J. Lamsal, Y. Lee, V.K. Anand, A. Kreyssig, T.W. Heitmann, R.J. McQueeney, A.I. Goldman, B.N. Harmon, A. Kaminski, D.C. Johnston, Phys. Rev. Lett. **108** 087005 (2012)

[4] D.P. Chen and C. T. Lin, Supercond. Sci. Technol. **27** (2014) 103002

[5] J.-K Bao, H. Jiang, Y.-L Sun, W.-H Jiao, C.-Y Shen, H.-J. Guo, Y. Chen, C.-M. Feng, H.-Q. Yuan, Z.-A. Xu, G.-H. Cao, R. Sasaki, T. Tanaka, K. Matsubayashi, Y. Uwatoko PRB **85**, 144523, (2012)

[6] L. Li, Y. K. Luo, Q,B, Wang, H. Chen, Z. Ren, Q. Tao, Z.A. Xu, New J. Phys. **11**, 025008, 2009

[7] Leithe-Jasper et. al. Phys. Rev. Lett. **101**, 207004 (2008)

[8] N. Kurita et.al. Phys. Rev. Lett. **102**. 147004 (2009)

[9] S. Lee, J. Jiang, Z. Zhaong, C.W. Bark, J.D. Weiss, C. Tarantini, C.T. Nelson, H.W. Jang, C.M. Folkman, S.H. Baek, A. Polyanskii, D. Abraimov, A. Yamamoto, J,W. Park, X.Q. Pan, E.E. Hellstrom, D.C. Larbalestrer, C.B. Eom, Nature Materials, **9**, 397-402 (2010)

[10] M. Rotter, M. Pangerl, M. Tegel, D. Hohrendt, Angew. Chem. Int. Ed. **47** 7949-7952, 2008

[11] D.E. McNally, S. Zeliman, Z.P. Yin, K.W. Post, Hua K. Hao, G. Koltiar, D. Basov, C.C. Homes and M.C. Aronsson, Phys. Rev. B **92**, 115142 (2015)

[12] M. Ramazanoglu, A. Sapkota, A. Pandey, J.Lamsal, D.L. Abernathy, J.L. Niedziela, M.B. Stone, A.Kressig, A.I.

Goldman, D.C. Johnston, R.J. McQueeney, Phys. Rev. B. **95**, 224401, (2017)

[13] R.J. McQueeney, J,-Q. Yan, S. Chang, J. Ma, Phys. Rev. B **78**, 184417 (2008)

[14] B. Lake, A. Aeppli, T.E. Mason, A. Schroder, D.F. Mc-Morrow, K. Lefmann, M. Isshiki, M. Nohara, H. Takagi, S. M. Hayden , Nature, Vol. **400**, 43, (1999)

[15] J. Lamsal, G.S. Tucker, T.W. Heitmann, A. Kreyssig, A. Jesche, A. Pandey, W. Tian, R. J. McQueeney, D.C. Johnston, A.I. Goldman, Phys. Rev. B **87** 144418 (2013)

[16] S. Jiang, H. Xing, G. Xuan, C. Wang, Z. Ren, C. Feng, J. Dai, Z. Xu, G. Cao, J. Phys.: Condens. Matter **21** (2009) 382203

[17] Sefat et. al. Phys. Rev. Lett. **101**, 117004 (2008)

[18] Alireza, Y.T. Chris Ko, J. Gillet, C. M. Petrone, J. M. Cole, G. G. Lonzarich , S. E. Sebestian, J. Phys. Condens. Matter **21** (2009) 021208

[19] Q. Huang, Y. Qiu, W. Bao, M.A. Green, J.W. Lynn, Y.C. Gasparovic, T. Wu, G. Wu, X. H. Chen, Phys. Rev. Lett. **101**, 257003 (2008)

[20] A free analysis software presented by NCNR, NIST.

[21] M. Kohgi, Y. Ishikawa, Y. Endoh, Solid State Commun., **11**, 391, (1972)

[22] Pavel Balaz, Jozef Barnas, Phys. Rev. B **91**, 104415 (2015)

[23] T.G. Perring, D.T. Adroja, G. Chaboussant, G. Aeppli, T. Kimura, Y. Tokura, Phys. Rev. Lett. **87**, 217201 (2001)

[24] J. Zhao, D.T. Adroja, D.-X. Yao, R. Bewley, S. Li, X.F. Wang, G. Wu, X.H. Chen, J. Hu, P. Dai, Nature Physics Vol.5, Issue 8, p555-560 (2009)

[25] F.Ye, P. Dai, J.A. Fernandez-Baca, D.T. Adroja, T.G. Perring, Y. Tomioka, T. Tokura, Phts. Rev. B **75**, 144408 (2007)

[26] P. Dai, H.Y. Hwang, J. Zhang, J.A. Fernandez-Baca, S.-W. Cheong, C. Kloc, Phys. Rev.B **61** 9553 (2000)
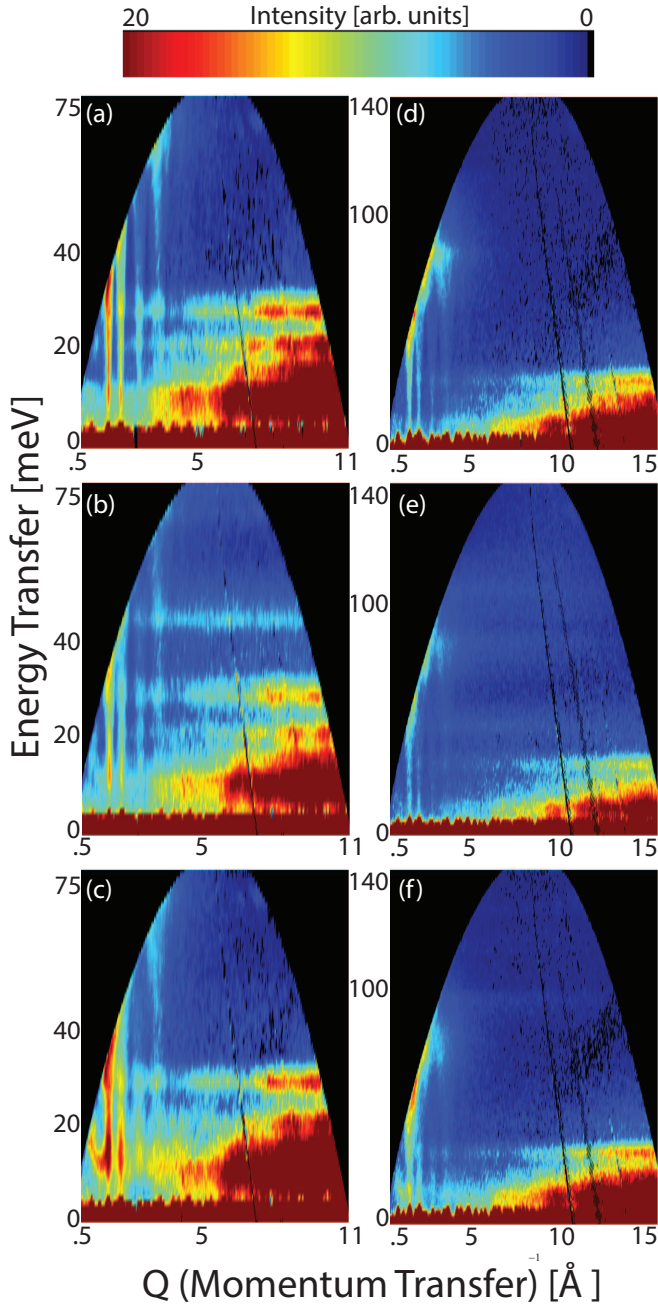
[27] www.ill.eu/sites/FULLPROF

Figure 1: Inelastic neutron scattering data from undoped and K doped powders of $BaMn_2As_2$. The panels on the left (a,b,c) show E_i =74 meV data while the ones on the right (d,e,f) show E_i =144.7 meV. Panel a and d, b and e , and c and f are created for parent, 12.5 % K doped and 25 % K doped powders of $BaMn_2As_2$, respectively. The profiles of INS data shown here are obtained after empty Al sample cell correction (the Al can scattering is subtracted from the detector data) is done for each sample. The intensity bar which is drawn on the top of this figure is valid for this figure and all other $3D$ figures in this article.
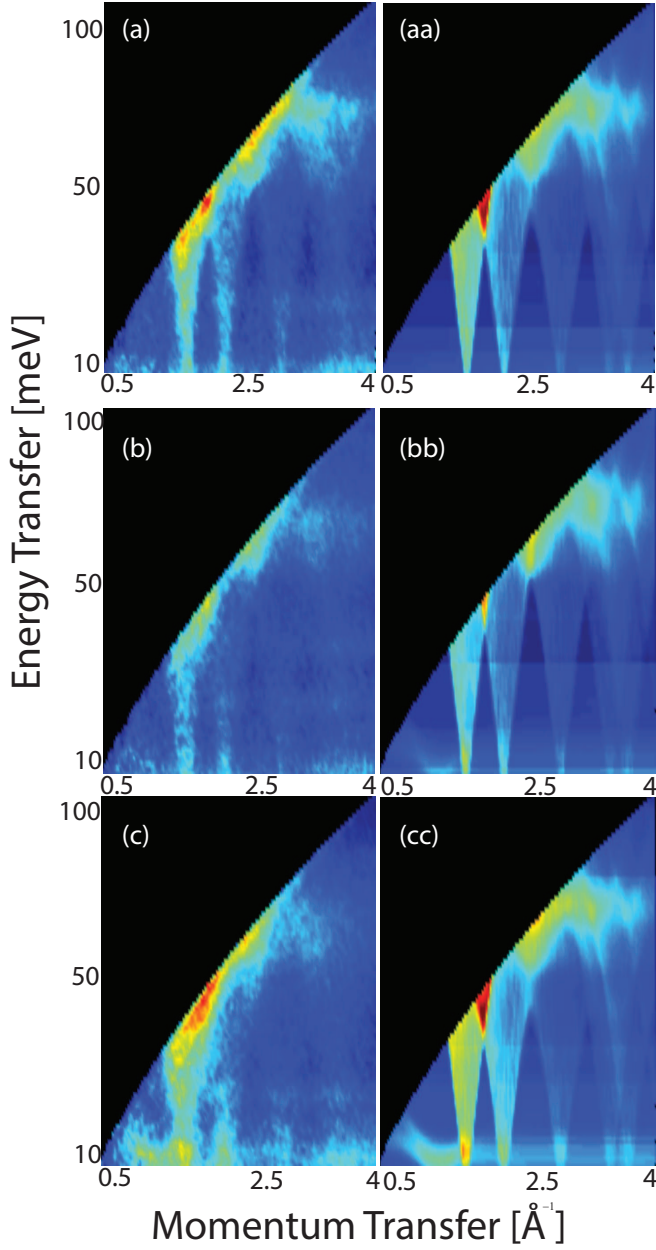
Figure 2: Low-q inelastic neutron scattering data from powders of parent $BaMn_2As_2$ in panel (a) and K doped $Ba_{(1-x)}K_xMn_2As_2$ in panels (b) and (c) with the corresponding simulations in panels (aa), (bb) and (cc), respectively. K concentrations are x=0.125 and x=0.25 respectively in panels (b) and (c) and all of the data are obtained for incident energy of E_i =144.7 meV. Panels on the right show the Heisenberg model calculations of neutron intensities using linear spin wave theory for corresponding powders. The intensities on these reflections were simulated by the calculations of the Heisenberg Spin Hamiltonian as explained in the text, shown in panels of (aa, bb and cc) are in good agreement. There is an extra scattering due to the MnO impurities at the low q and low E side of the data. This is weakly seen for 12.5% but more pronounced for 25% K doped sample. The results of calculations of AFM spin wave scattering for MnO impurities in the powder samples were included in the model. The same intensity scale -color-bar- used in Fig.1 is used in this figure.
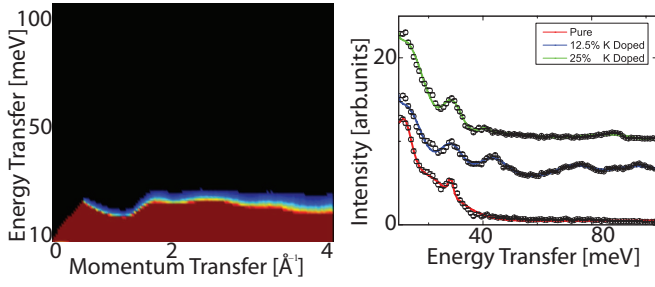
Figure 3: Magnetic spin-wave powder neutron scattering intensity calculation for MnO powder in panel (a) and phonon scattering averaged intensity over Q=[6:8] Å^{-1} range versus energy transfer up to ~ 100 meV range in panel (b). MnO powder calculation is drawn over the same q, E range as shown in Fig.2. The phonon intensities are fitted to a line shape which involves several Gaussian. The line shape is used to create a $3D$ background which is used with appropriate scaling to define the background of the analysis especially for the range of E$\leq$50 meV. The MnO powder intensities are used mainly to define the extra scattering in the low q and low E range. A scaling of $\sim 1/400$ and $\sim 1/150$ is used for 12.5 % and 25 % K doped samples,respectively. This calculated background for MnO is added to the $\sim q^2$ background fit results in the range of 10 meV$\leq$E$\leq$50 meV as explained in the text. The same intensity scale used in Fig.1 is used for the left panel of this figure, as well.
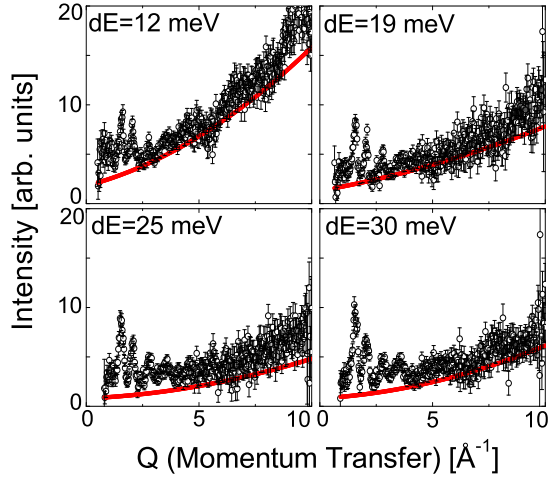
Figure 4: Four different representative figures for phonon background fit analysis. The panels show the quadratic $\sim q^2$ behaviour for parent $BaMn_2As_2$ INS data.
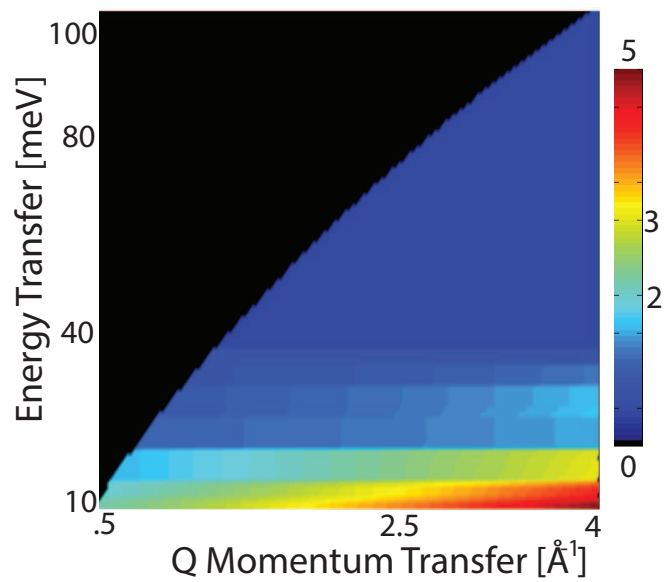
Figure 5: Background data used for the parent BaMn$_2$As$_2$ analysis. As seen here, a monotonically decreasing intensity is observed from energy transfer values from E=10 meV to E∼40 meV. As the momentum transfer increases, the increase in the intensity for the low energy transfer range is due to the quadratic background estimation, explained in the text.
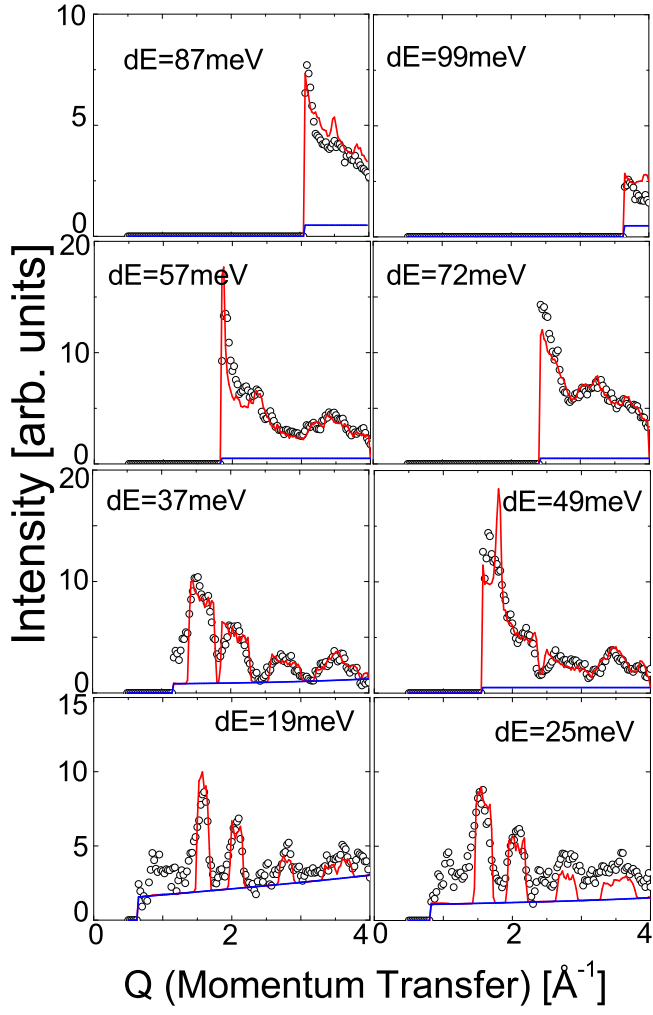
Figure 6: Eight different energy cuts of powder neutron intensity analysis for undoped $BaMn_2As_2$ sample. The q dependence of background and the overall fit is drawn using blue and red circles, respectively. The blue line is obtained by quadratic q dependent phonon fits especially within the E$\leq$ 50 meV range. Above this energy, the background is estimated by Gaussian fits, shown in the Fig. 3. This yields usually small but constant intensity values up to E=104 meV.
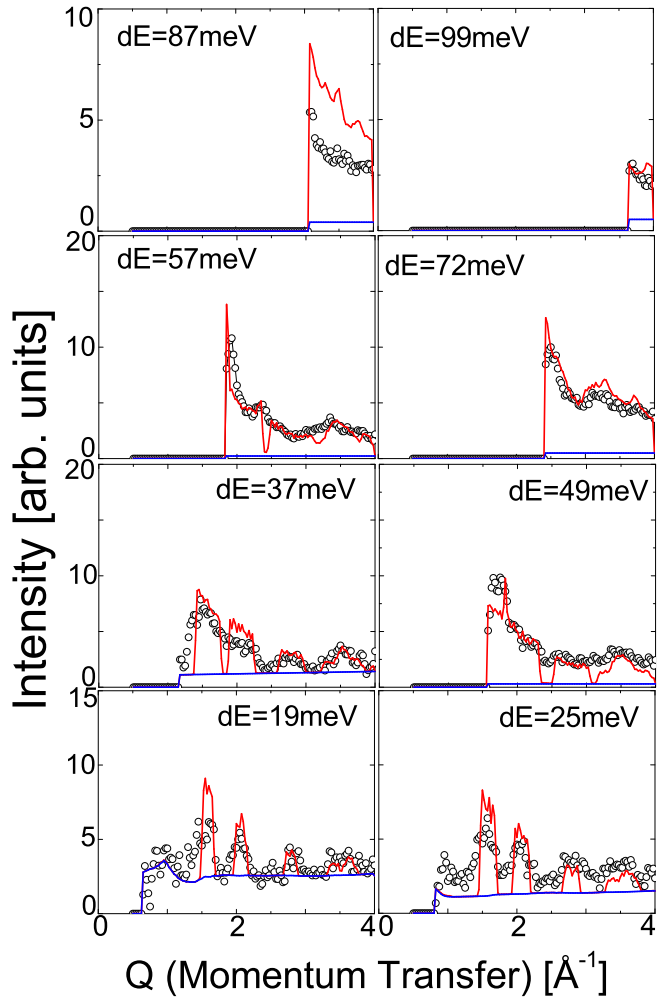
Figure 7: Eight different energy cuts of powder neutron intensity analysis for 12.5 % K doped powder sample; $Ba_{0.875}K_{0.125}Mn_2As_2$. The q dependence of background and the overall fit is drawn using blue and red circles, respectively. As it is seen for the low energy transfer values and q$\sim$1Å^{-1}, a clear extra intensity is seen, originating from calculated from MnO powder analysis.
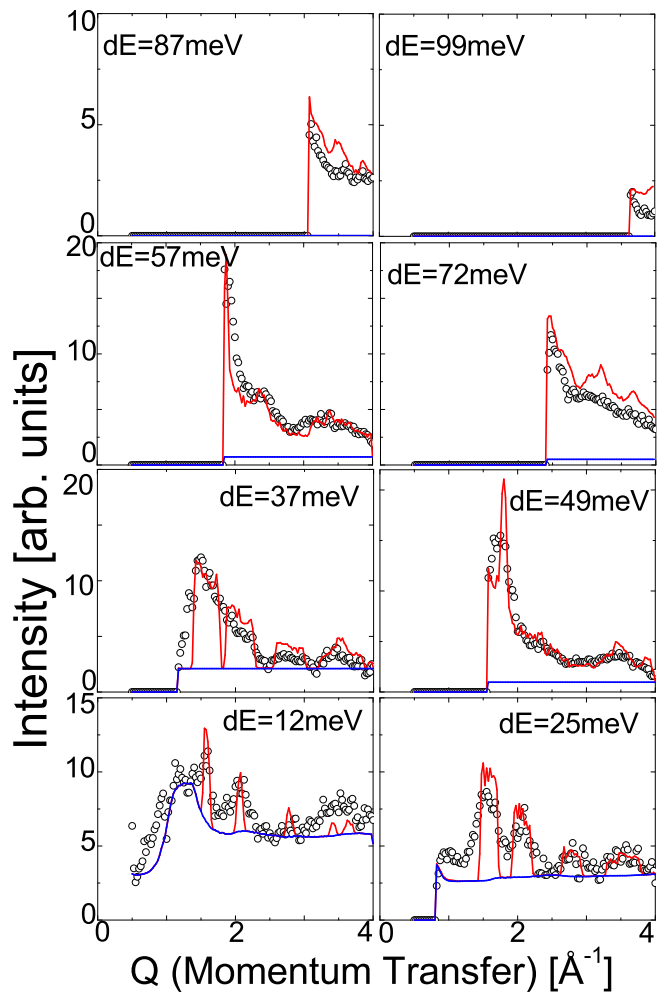
Figure 8: Eight different energy cuts of powder neutron intensity analysis for 25 % K doped powder sample; $Ba_{.75}K_{.25}Mn_2As_2$. The q dependence of background and the overall fit is drawn using blue and red circles, respectively. In the lowest energy cut panel, the MnO intensity draws the lowest q peak and this intensity quickly drops for the next energy panel.
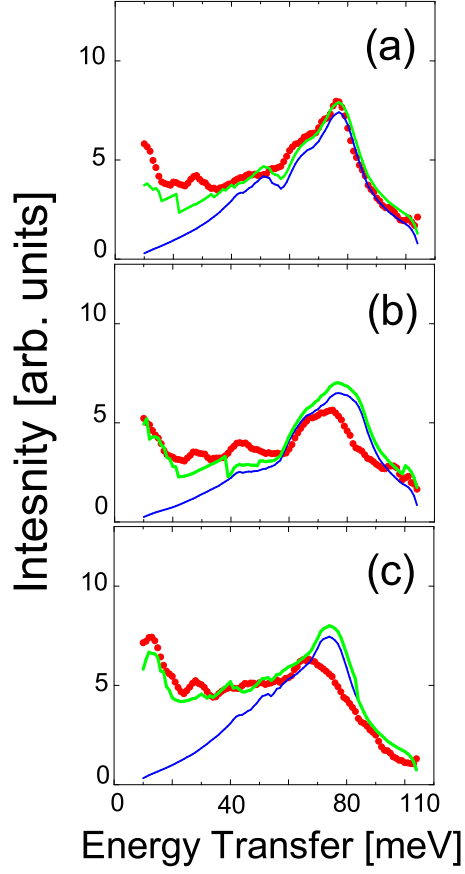
Figure 9: Powder magnetic neutron inelastic intensities versus energy transfer profile with binned and averaged over whole momentum transfer range. The red colored data are the momentum transfer .averaged S(q,E) intensities obtained from the data shown in the Fig. 2. Blue colored lines are the results of the Heisenberg Spin Model analysis without any background while the green continuous lines are the ones added with the background information. The good agreement between the green, representing the total analysis including the background estimation with MnO scattering addition, and the red line, the raw data, can be seen especially for the low-E regions.
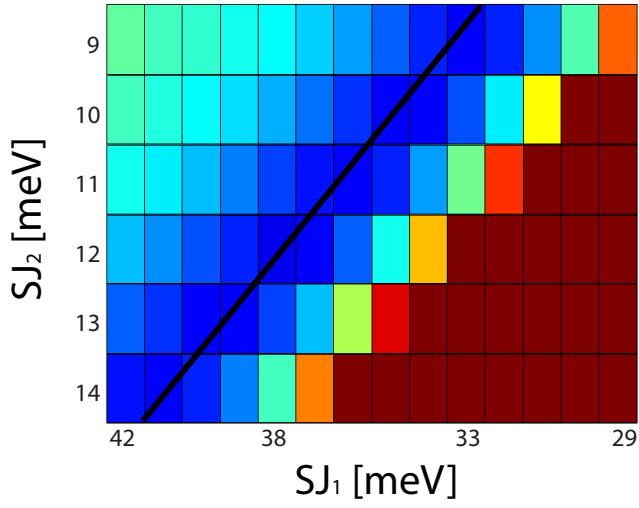
Figure 10: Goodness of the fit, χ^2 with respect to different magnetic exchange constant values shown for parent compound BaMn$_2$As$_2$. The S(q,E) was calculated for a set of SJ$_1$ and SJ$_2$ with the values given in the x and y axes in the figure using the Heisenberg model spin-wave analysis as explained in the text. In this figure, SJ$_z$ $\sim$2 meV. Red color shows the high values of χ^2, while blue shows the low values. As can be seen, a linear low chi-square valley like behaviour shown by a continuous black line is observed. Similar behaviour is also observed in the doped samples as well with different values of SJ$_s$. The black line is estimated as SJ$_1 \simeq \frac{3}{2}$SJ$_2$-15+0.8SJ$_z$.
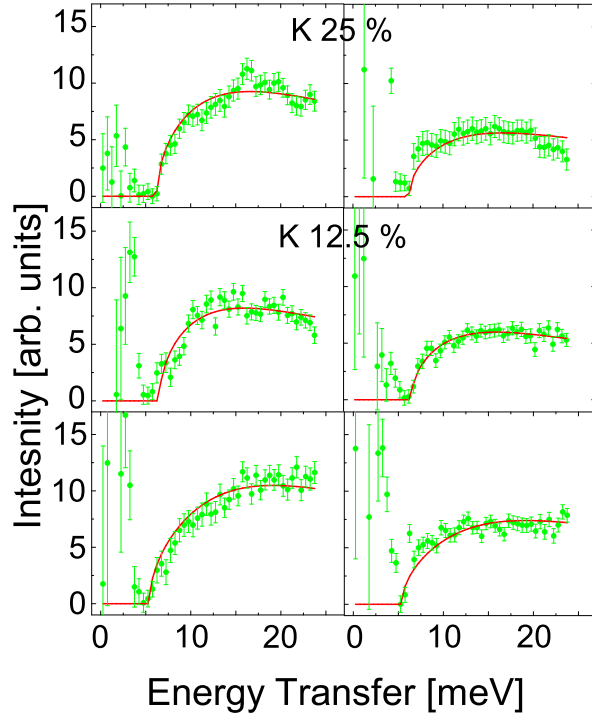
Figure 11: Two different constant q-cut profiles, obtained from E_i =144.7 meV data, drawn for I vs E energy transfer up-to ~25 meV for different K concentrations. These constant q-spectra which are shown on the left panels were obtained for q=1.575Å^{-1} while right panels are for q=2.04Å^{-1}. The data preparation and the details of the lineshape analysis are explained in the text. The red colored fit lines have common fit parameter values obtained from global fits to the data at two q-reflections. These values are given in Table II
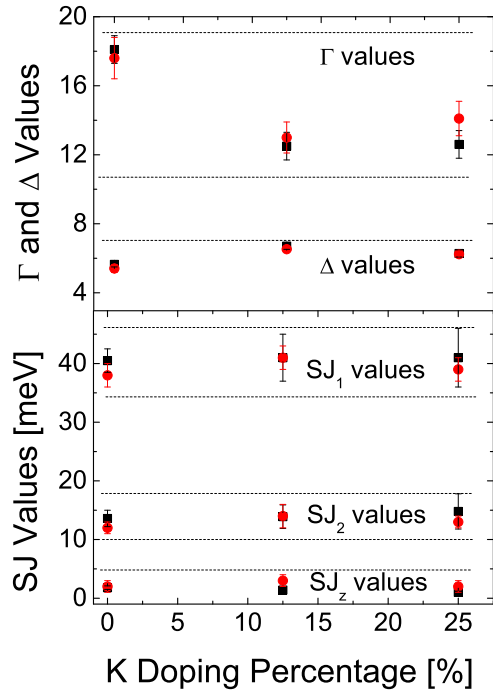
.

Figure 12: Comparison between the current and previous analysis [12]. Black squares and red circles show the best values of the fit parameters of previous [12] and current results, respectively.